Frontiers of Information Technology & Electronic Engineering
www.jzus.zju.edu.cn; engineering.cae.cn; www.springerlink.com
ISSN 2095-9184 (print); ISSN 2095-9230 (online)
E-mail: jzus@zju.edu.cn

Realizing complex beams via amplitude-phase digital coding metasurfaces and semidefinite relaxation optimization*#

Junwei WU[1,2,3], Qiong HUA[1], Hui XU[1], Hanqing YANG[1],
Zhengxing WANG[1], Qiang CHENG[†‡1], Tie Jun CUI[†‡1,2,3]

[1]*State Key Laboratory of Millimeter Waves, Southeast University, Nanjing 210096, China*

[2]*Peng Cheng Laboratory, Shenzhen 518055, China*

[3]*Pazhou Laboratory (Huangpu), Guangzhou 510555, China*

[†]E-mail: qiangcheng@seu.edu.cn; tjcui@seu.edu.cn

Received Mar. 1, 2023; Revision accepted July 4, 2023; Crosschecked Aug. 1, 2023

Abstract: Complex beams play important roles in wireless communications, radar, and satellites, and have attracted great interest in recent years. In light of this background, we present a fast and efficient approach to realize complex beams by using semidefinite relaxation (SDR) optimization and amplitude-phase digital coding metasurfaces. As the application examples of this approach, complex beam patterns with cosecant, flat-top, and double shapes are designed and verified using full-wave simulations and experimental measurements. The results show excellent main lobes and low-level side lobes and demonstrate the effectiveness of the approach. Compared with previous works, this approach can solve the complex beam-forming problem more rapidly and effectively. Therefore, the approach will be of great significance in the design of beam-forming systems in wireless applications.

Key words: Antenna beams; Amplitude-phase coding metasurface; Far-field synthesis; Semidefinite relaxation
https://doi.org/10.1631/FITEE.2300146 **CLC number:** TN820

1 Introduction

Complex antenna beams have particular applications in wireless systems. For instance, the cosecant beams in reconnaissance radars compensate for the propagation loss at different distances and maintain the received power constant (Balanis, 2011), and the flat-top beam in a cellular network provides a uniform signal level and thus improves the coverage in the service area (Palacios et al., 2016). Traditional phased-array antennas can be used to achieve complex beam patterns, but they are not convenient due to the complicated radio frequency (RF) modules. On the other hand, electromagnetic metasurfaces (Cui et al., 2017) have attracted extensive attention in recent years because of their simple structure and strong capability. In particular, they can flexibly control the electromagnetic wavefront and have found various applications (Wu et al., 2020, 2021; Liang et al., 2022; Lou et al., 2023; Sun et al., 2023). Therefore, using electromagnetic metasurfaces is a reasonable way to generate complex beams.

The design of complex beams is actually an array synthesis problem, which aims to find the excitation vector of the array that meets the expected far-

‡ Corresponding authors

* Project supported by the National Key Research and Development Program of China (Nos. 2021YFA1401002 and 2018YFA070194), the National Natural Science Foundation of China (Nos. 62171124, 62288101, and 62225108), the Major Key Project of Peng Cheng Laboratory, China (No. PCL2023AS1-2), the 111 Project, China (No. 111-2-05), the Jiangsu Provincial Frontier Leading Technology Basic Research Project, China (No. BK20212002), the Fundamental Research Funds for the Central Universities, China (No. 2242023k5002), and the Jiangsu Provincial Innovation and Entrepreneurship Doctor Program, China

Electronic supplementary materials: The online version of this article (https://doi.org/10.1631/FITEE.2300146) contains supplementary materials, which are available to authorized users

ORCID: Junwei WU, https://orcid.org/0000-0001-9764-1178; Qiang CHENG, https://orcid.org/0000-0002-2442-8357; Tie Jun CUI, https://orcid.org/0000-0002-5862-1497

field characteristics and criteria. Many effective approaches have been proposed in the past few decades to solve array synthesis problems. Analytical approaches such as Dolph–Chebyshev (Dolph, 1946) and Taylor (Li et al., 2017) syntheses can realize far-field beam patterns with low side lobe levels, but they are suitable only for linear arrays with equal spacing and few elements. Stochastic optimization methods like differential evolution (DE) (Caorsi et al., 2005), particle swarm optimization (PSO) (Khodier and Christodoulou, 2005), and genetic algorithm (GA) (Shi et al., 2012) have been widely used. Although these methods have significant universality and flexibility, their disadvantages are obvious, such as slow convergence, extensive computations, or even prohibitive costs. The alternative projection approach (Bucci et al., 1994) features high computational efficiency. However, it may be trapped by local minima due to the nonconvexity of the optimization problem.

Convex optimization is an important branch of the optimization field, and it has been studied extensively in combination with the design of antenna beams (Lebret and Boyd, 1997; Nai et al., 2010; Tsui and Chan, 2010; Yang et al., 2018; Wu et al., 2023). Once the array synthesis problem is expressed in convex form, the optimal solution can be obtained by using a readily available tool (Grant and Boyd, 2020). However, most synthesis problems of complex beam patterns are concave, which hinders the direct application of convex optimization. The semidefinite relaxation (SDR) technique can be used to deal with the non-convex synthesis problem (Wang et al., 2003; Kajenski, 2012). The point of SDR is relaxation, which means removing the concave restriction from the original problems. Feasible solutions to difficult optimization problems can be found effectively by using SDR. In this work, an iterative method based on SDR is described to solve complex beam-forming problems, and amplitude-phase coding metasurfaces based on C-shaped structures are designed to verify the effectiveness of the method (Bao et al., 2019). The weighting vectors satisfying the expected far-field patterns, including the cosecant, flat-top, and double beams, can be obtained in a few seconds. Full-wave simulations and experimental measurements of the fabricated metasurface are performed, and the results verify that the numerical method and the realization approach are effective and feasible.

2 Method

2.1 Antenna array

Consider a uniform and N-element linear array with the n^{th} element located at $(x_n,\ 0,\ 0)$ in the Cartesian coordinates. The corresponding far field is

$$G(\theta)=\sum_{n=1}^{N}E_n w_n \mathrm{e}^{\mathrm{j}\frac{2\pi}{\lambda}x_n\sin\theta}, \tag{1}$$

where θ is the angle between the observation point and the positive z axis, w_n is the complex weight of the n^{th} element, and λ is the wavelength. E_n is the far field of the n^{th} element in the θ direction, and it will be simplified to 1 in this study. We can rewrite Eq. (1) as follows:

$$\boldsymbol{w}=[w_1,w_2,\ldots,w_N], \tag{2}$$

$$\boldsymbol{v}(\theta)=\left[\mathrm{e}^{\mathrm{j}kx_1\sin\theta},\mathrm{e}^{\mathrm{j}kx_2\sin\theta},\ldots,\mathrm{e}^{\mathrm{j}kx_N\sin\theta}\right]^{\mathrm{T}}, \tag{3}$$

$$G(\theta)=\boldsymbol{w}\boldsymbol{v}(\theta). \tag{4}$$

By separating the real and imaginary parts of the complex vector $\boldsymbol{w}$, we obtain a new vector:

$$\begin{aligned}\boldsymbol{x}=&[R(w_1),R(w_2),\ldots,R(w_N),\\&I(w_1),I(w_2),\ldots,I(w_N)]^{\mathrm{T}},\end{aligned} \tag{5}$$

where $R(\cdot)$ and $I(\cdot)$ represent the real and imaginary parts, respectively. In the same way, we separate $\boldsymbol{v}(\theta)$ to obtain two new vectors:

$$\begin{aligned}\boldsymbol{a}(\theta)=&[R(v_1),R(v_2),\ldots,R(v_N),\\&-I(v_1),-I(v_2),\ldots,-I(v_N)],\end{aligned} \tag{6}$$

$$\begin{aligned}\boldsymbol{b}(\theta)=&[I(v_1),I(v_2),\ldots,I(v_N),\\&R(v_1),R(v_2),\ldots,R(v_N)],\end{aligned} \tag{7}$$

where v_n ($n=1, 2, \ldots, N$) is the n^{th} element of $\boldsymbol{v}(\theta)$. Now we can express the far-field power as

$$|G(\theta)|^2=\boldsymbol{x}^{\mathrm{T}}\overline{\boldsymbol{U}}^{\mathrm{T}}\overline{\boldsymbol{U}}\boldsymbol{x}, \tag{8}$$

where

$$\overline{\boldsymbol{U}}=[\boldsymbol{a},\quad \boldsymbol{b}]^{\mathrm{T}}. \tag{9}$$

According to the linear algebra theory (Strang, 2023), we know that for any N-dimensional real-row vector $\boldsymbol{y}$ and any $N\times N$ real matrix $\overline{\boldsymbol{A}}$, the following relationship holds:

$$\boldsymbol{y}^{\mathrm{T}}\overline{\boldsymbol{A}}\boldsymbol{y}=\mathrm{tr}\left(\boldsymbol{y}^{\mathrm{T}}\overline{\boldsymbol{A}}\boldsymbol{y}\right)=\mathrm{tr}\left(\overline{\boldsymbol{A}}\boldsymbol{y}\boldsymbol{y}^{\mathrm{T}}\right), \tag{10}$$

where $\mathrm{tr}(\cdot)$ stands for the trace of a matrix. Therefore, we can rewrite Eq. (8) as

$$\begin{aligned}|G(\theta)|^2 =&\boldsymbol{x}^{\mathrm{T}}\overline{\boldsymbol{P}}\boldsymbol{x}=\mathrm{tr}\left(\boldsymbol{x}^{\mathrm{T}}\overline{\boldsymbol{P}}\boldsymbol{x}\right)=\mathrm{tr}\left(\overline{\boldsymbol{P}}\boldsymbol{x}\boldsymbol{x}^{\mathrm{T}}\right)\\ =&\mathrm{tr}(\overline{\boldsymbol{P}}\,\overline{\boldsymbol{X}}),\end{aligned}\tag{11}$$

where

$$\overline{\boldsymbol{X}}=\boldsymbol{x}\boldsymbol{x}^{\mathrm{T}},\tag{12}$$

and

$$\overline{\boldsymbol{P}}=\overline{\boldsymbol{U}}^{\mathrm{T}}\overline{\boldsymbol{U}}\tag{13}$$

is the direction matrix of θ. Note that Eq. (12) means that $\overline{\boldsymbol{X}}$ is a symmetric positive semidefinite matrix whose rank is 1.

2.2 Semidefinite relaxation

We consider an optimization problem in the following form:

$$\begin{aligned}&\min_{\boldsymbol{z}\in\mathbb{R}^M}\quad \boldsymbol{z}^{\mathrm{T}}\overline{\boldsymbol{C}}\boldsymbol{z}\\ &\text{s.t.}\quad \boldsymbol{z}^{\mathrm{T}}\boldsymbol{z}\nabla b_n,\quad n=1,2,\dots,N,\end{aligned}\tag{14}$$

where $\overline{\boldsymbol{C}}$ is an $M\times M$ real matrix, ∇ means $\geq$, $=$, or $\leq$, and b_n represents an arbitrary real number. The above problem aims to find the minimum value of $\boldsymbol{z}^{\mathrm{T}}\overline{\boldsymbol{C}}\boldsymbol{z}$ among all $\boldsymbol{z}$'s that satisfy the constraints. In general, the problem is difficult and nondeterministic polynomial (NP) hard. To solve it, a new variable matrix $\overline{\boldsymbol{Z}}=\boldsymbol{z}\boldsymbol{z}^{\mathrm{T}}$ is introduced. $\overline{\boldsymbol{Z}}$ is an $M\times M$ symmetric positive semidefinite matrix and its rank is 1. According to Eqs. (10) and (12), problem (14) can be rewritten as follows:

$$\begin{aligned}&\min_{\overline{\boldsymbol{Z}}\in S^M}\ \mathrm{tr}(\overline{\boldsymbol{C}}\,\overline{\boldsymbol{Z}})\\ &\text{s.t.}\ \ \mathrm{tr}\left(\overline{\boldsymbol{C}}_n\overline{\boldsymbol{Z}}\right)\nabla b_n,\quad n=1,2,\dots,N,\\ &\quad\ \overline{\boldsymbol{Z}}\geq 0,\quad \mathrm{rank}(\overline{\boldsymbol{Z}})=1,\end{aligned}\tag{15}$$

where S denotes the set of symmetric positive semidefinite matrices, and $\overline{\boldsymbol{Z}}\geq 0$ means that $\overline{\boldsymbol{Z}}$ is a symmetric positive semidefinite matrix. In the above problem, only the rank-one constraint is non-convex, and thus we remove it and obtain a new optimization problem:

$$\begin{aligned}&\min_{\overline{\boldsymbol{Z}}\in S^M}\ \mathrm{tr}(\overline{\boldsymbol{C}}\,\overline{\boldsymbol{Z}})\\ &\text{s.t.}\,\mathrm{tr}\left(\overline{\boldsymbol{C}}_n\overline{\boldsymbol{Z}}\right)\nabla b_n,\ n=1,2,\dots,N,\ \overline{\boldsymbol{Z}}\geq 0.\end{aligned}\tag{16}$$

The above expression is the SDR (Luo et al., 2010) form of problem (15). The problem is now strictly convex (Boyd and Vandenberghe, 2004), and we can then use the CVX toolbox to obtain the solution $\overline{\boldsymbol{Z}}^*$. Note that the local solution of a convex problem is also globally optimal, which is an excellent property for convex optimization.

Problems (15) and (16) are equivalent only if the rank of $\overline{\boldsymbol{Z}}^*$ is 1. This is the best case, under which problem (15) has an optimal solution. However, the interior point method usually leads to a solution with the rank larger than 1. To find the optimal solution to problem (15), or to make the rank of $\overline{\boldsymbol{Z}}^*$ equal to 1, we here adopt an iterative optimization algorithm (Fazel et al., 2004). The idea is to obtain a minimum rank of a matrix by minimizing its trace, which is known as the rank minimization solution theory. Therefore, an extra objective function is added to problem (16) as

$$\begin{aligned}&\min_{\overline{\boldsymbol{Z}}^k\in S^M}\ \mathrm{tr}\left(\overline{\boldsymbol{C}}\,\overline{\boldsymbol{Z}}^k\right)+\zeta\,\mathrm{tr}\left(\left(\overline{\boldsymbol{Z}}^{k-1}+\delta\overline{\boldsymbol{I}}\right)^{-1}\overline{\boldsymbol{Z}}^k\right)\\ &\quad\text{s.t.}\,\mathrm{tr}\left(\overline{\boldsymbol{C}}_n\,\overline{\boldsymbol{Z}}^k\right)\nabla b_n,\ n=1,2,\dots,N,\ \overline{\boldsymbol{Z}}^k\geq 0,\end{aligned}\tag{17}$$

where k is the number of iterations, δ is a small positive constant, ζ is a constant between 0 and 1, $\overline{\boldsymbol{I}}$ is the identity matrix of $M\times M$, and $\overline{\boldsymbol{Z}}^0=\overline{\boldsymbol{I}}$. If the rank of $\overline{\boldsymbol{Z}}_1^*$ obtained by problem (17) is 1, we obtain the optimal solution to Eq. (15). Otherwise, an approximation solution to the original problem can be found by the method of eigenvalue decomposition:

$$\overline{\boldsymbol{Z}}_2^*=\sigma_1\boldsymbol{u}_1\boldsymbol{u}_1^{\mathrm{T}},\tag{18}$$

$$\boldsymbol{z}_2^*=\sqrt{\sigma_1}\boldsymbol{u}_1,\tag{19}$$

where σ_1 is the maximum eigenvalue of $\overline{\boldsymbol{Z}}_1^*$, and $\boldsymbol{u}_1$ is the corresponding eigenvector. $\overline{\boldsymbol{Z}}_2^*$ is thus regarded as the feasible solution to problem (15). Therefore, we obtain the appropriate solution $\boldsymbol{z}_2^*$ to problem (14) by eigenvalue decomposition.

Up to now, we have solved the non-convex optimization problem by using SDR, rank minimization theory, and eigenvalue decomposition. The key steps are summarized as follows: the convex problem is obtained by dropping the rank-one constraint. Once the rank of the solution to the SDR problem is one, the optimal solution to the original problem is found. Otherwise, an iterative approach is adopted to solve the problem. If the rank-one solution still cannot be found, we will obtain the approximate solution to

the original problem through eigenvalue decomposition. The flowchart to solve problem (14) is shown in Fig. 1.

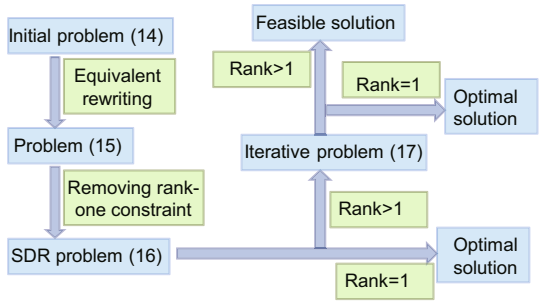

Fig. 1 Key steps to solve problem (14)

2.3 Exemplary complex beam-forming problems

We here present exemplary applications of the above method in determining the weighting vector of complex beams. Generally, the intended beam patterns should satisfy the following constraints: an upper boundary for the side lobe level and a double-boundary constraint for the main lobe. For instance, the side lobe level is below −20 dB, while the level of the main lobe region fluctuates within [−0.5, +0.5] dB.

2.3.1 Cosecant and flat-top beams

The problem of synthesizing cosecant and flat-top beams is formulated as follows:

$$\begin{aligned}&\text{find } \boldsymbol{w}\\&\text{s.t. } l(\theta_i)\le\left|G(\theta_i)\right|^2\le u(\theta_i),\\&\qquad\qquad\theta_i\in\mathrm{ML}\ (i=1,2,\ldots,I),\\&\left|G(\theta_j)\right|^2\le\rho(\theta_j),\quad\theta_j\in\mathrm{SL}\ (j=1,2,\ldots,J),\end{aligned}\tag{20}$$

where I and J are the numbers of directions in the main lobe and side lobe regions respectively, $l(\theta_i)$, $u(\theta_i)$, and $\rho(\theta_j)$ are all positive constants, and ML and SL represent the sets of main lobe and side lobe directions respectively. In the above problem, the first inequality is the double-boundary constraint in the main lobe region, while the second inequality shows the maximum level of the side lobe region. In this work, the step of θ is set to 1°. According to the conversion method mentioned in Section 2.2, the above problem can be rewritten as

$$\begin{aligned}&\text{find } \overline{\boldsymbol{X}}\\&\text{s.t. } l(\theta_i)\le\mathrm{tr}\left(\overline{\boldsymbol{P}}_i\,\overline{\boldsymbol{X}}\right)\le u(\theta_i),\\&\qquad\qquad\theta_i\in\mathrm{ML}\ (i=1,2,\ldots,I),\\&\mathrm{tr}\left(\overline{\boldsymbol{P}}_j\overline{\boldsymbol{X}}\right)\le\rho(\theta_j),\ \ \theta_j\in\mathrm{SL}\ (j=1,2,\ldots,J),\end{aligned}\tag{21}$$

where $\overline{\boldsymbol{X}}$ is naturally a symmetric positive semidefinite matrix with rank one.

We obtain the SDR problem of problem (21) by removing the rank-one constraint and then solving the problem according to the method proposed in Section 2.1. The analogical form of problem (17) can be obtained by rewriting problem (21) as

$$\begin{aligned}&\min_{\overline{\boldsymbol{X}}^k\in S^M}\zeta\,\mathrm{tr}\left(\left(\overline{\boldsymbol{X}}^{k-1}+\delta\overline{\boldsymbol{I}}\right)^{-1}\overline{\boldsymbol{X}}^k\right)\\&\text{s.t. } l(\theta_i)\le\mathrm{tr}\left(\overline{\boldsymbol{P}}_i\,\overline{\boldsymbol{X}}^k\right)\le u(\theta_i),\\&\qquad\qquad\theta_i\in\mathrm{ML}\ (i=1,2,\ldots,I),\\&\mathrm{tr}\left(\overline{\boldsymbol{P}}_j\overline{\boldsymbol{X}}^k\right)\le\rho(\theta_j),\theta_j\in\mathrm{SL}\ (j=1,2,\ldots,J),\\&\overline{\boldsymbol{X}}^k\ge 0.\end{aligned}\tag{22}$$

Although there is no objective function in problem (20), it does not affect the usage of the above iterative algorithm. To simplify this optimization problem, ζ in problem (22) is set to 1. An optimal or feasible solution to problem (20) will be found finally through Eqs. (18) and (19) and problem (22).

2.3.2 Double beams

Inspired by the works of Lebret and Boyd (1997) and Bucci et al. (2002), the synthesis of double beams can be expressed as

$$\begin{aligned}&\text{find } \boldsymbol{w}\\&\text{s.t. }\left|G(\theta_1^*)\right|^2\ge 1,\ \left|G(\theta_2^*)\right|^2\ge 1,\\&l(\theta_i)\le\left|G(\theta_i)\right|^2\le u(\theta_i),\\&\qquad\qquad\theta_i\in\mathrm{ML}\ (i=1,2,\ldots,I),\\&\left|G(\theta_j)\right|^2\le\rho(\theta_j),\quad\theta_j\in\mathrm{SL}\ (j=1,2,\ldots,J),\end{aligned}\tag{23}$$

where θ_1^* and θ_2^* represent the central directions of the two beams to be formed. The above constraints are similar to those in problem (20). Problem (23) can be rewritten in the following form according to

Eqs. (2)–(4) and (11)–(13):

$$\begin{aligned}&\text{find}\ \ \boldsymbol{w}\\&\text{s.t.}\,\mathrm{tr}\left(\overline{\boldsymbol{P}}_1^{*}\,\overline{\boldsymbol{X}}\right)\geq 1,\ \mathrm{tr}\left(\overline{\boldsymbol{P}}_2^{*}\,\overline{\boldsymbol{X}}\right)\geq 1,\\&l\left(\theta_i\right)\leq \mathrm{tr}\left(\overline{\boldsymbol{P}}_i\,\overline{\boldsymbol{X}}\right)\leq u\left(\theta_i\right),\\&\qquad\qquad\theta_i\in \mathrm{ML}\ (i=1,2,\ldots,I),\\&\mathrm{tr}\left(\overline{\boldsymbol{P}}_j\,\overline{\boldsymbol{X}}\right)\leq \rho\left(\theta_j\right),\ \theta_j\in \mathrm{SL}\ (j=1,2,\ldots,J),\end{aligned}\tag{24}$$

where $\overline{\boldsymbol{P}}_1^{*}$ and $\overline{\boldsymbol{P}}_2^{*}$ are the direction matrices of the beams along θ_1^{*} and θ_2^{*}, respectively. Then the method in Section 2.1 is used to solve the problem.

3 Results

Numerical calculations, full-wave simulations, and experimental results are presented in this section. Fig. 2 shows the three-dimensional scenario of one of the designs. The working frequency is set as 16 GHz, and the distances between the array elements are all 5 mm, which is close to 1/4 wavelength. Such spacing is designed to yield metasurface elements with good amplitude and phase responses, and the purpose is not to obtain an angular resolution better than that of a regular array with element spacing of 1/2 wavelength.

3.1 Numerical results

The synthesis of the cosecant beam is performed first. A linear array composed of 25 isotropic elements is designed. The optimization goal is to achieve a cosecant beam with a low ripple in the main lobe region and a side lobe level that is as low as possible. The numerical results are shown in Fig. 3a with the black solid line. The cosecant beam is formed from 20° to 51° and the 0 dB main lobe points at 21°, while the side lobe level is almost below −30 dB in −90°–13° and 58°–90°. On the left and right sides of the main lobe region, there are two transition areas with a range of 6°. The corresponding weighting factors of the array are shown in Fig. 3b.

For the synthesis of a flat-top beam, the array is made up of 30 elements. The optimization results are presented as the black solid line in Fig. 4a. The main lobe area is −40°–4°. The left side lobe region is in −90°–−41° with a level less than −20 dB, and the right minor lobe is from −3° to 90° with a level less than −24 dB. The corresponding weighting factors of the array are shown in Fig. 4b.

For the synthesis of double beams, the array is

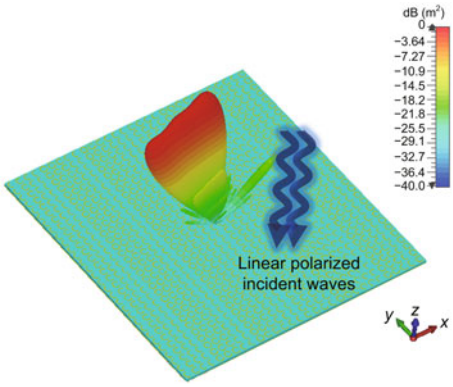

Fig. 2 Schematic of generating a flat-top beam by using an amplitude-phase digital coding metasurface. The incident wave is along the z direction, while the metasurface is in the xy-plane

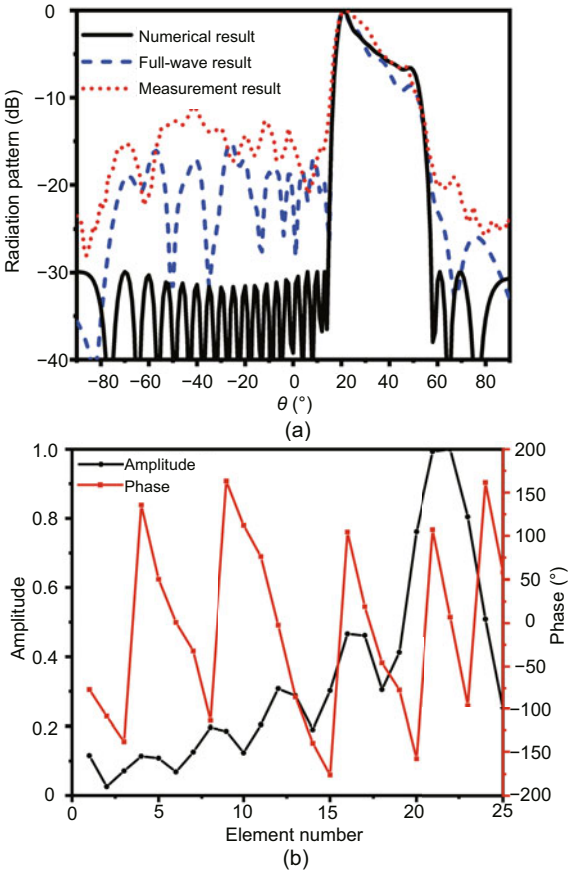

Fig. 3 Synthesis results of the cosecant beam: (a) numerically calculated, full-wave simulated, and experimentally measured beam patterns; (b) corresponding amplitude and phase of the array weighting vector. References to color refer to the online version of this figure

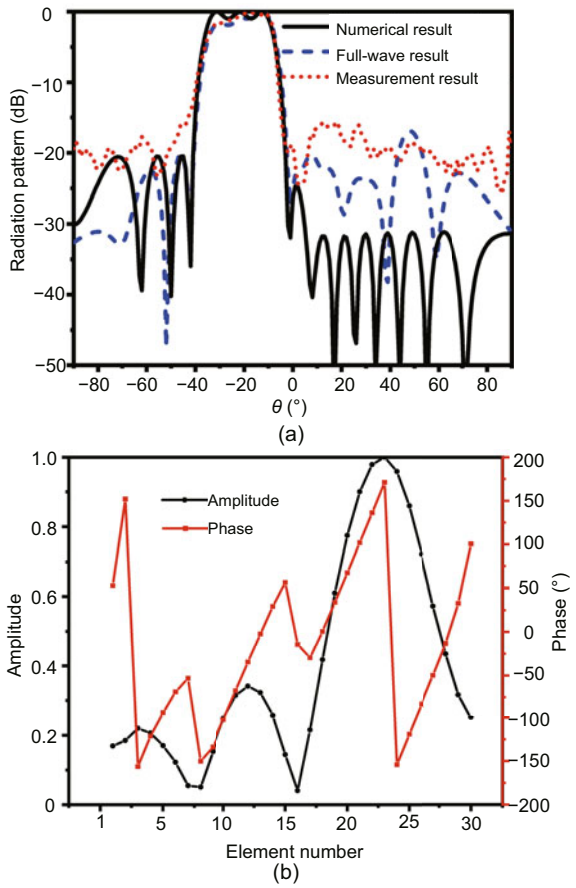

Fig. 4 Synthesis results of the flat-top beam: (a) numerically calculated, full-wave simulated, and experimentally measured beam patterns; (b) corresponding amplitude and phase of the array weighting vector. References to color refer to the online version of this figure

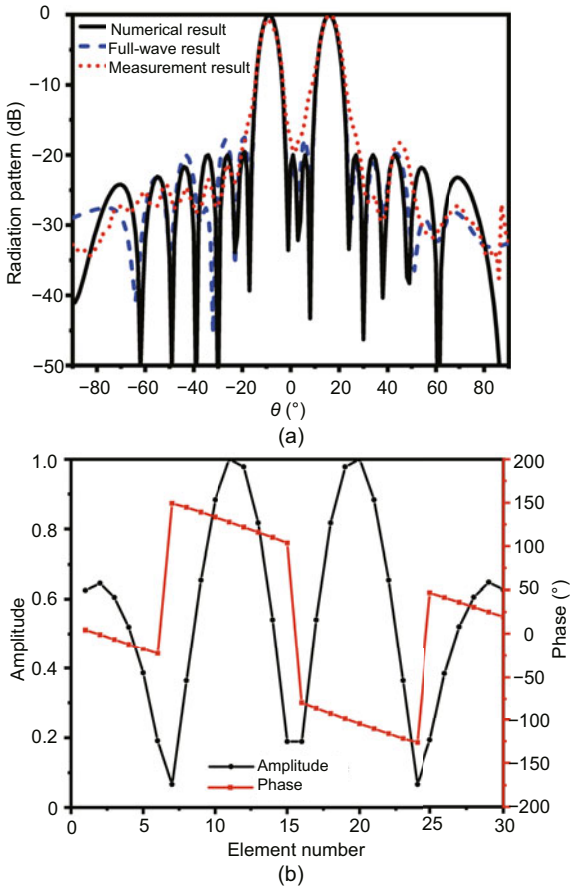

Fig. 5 Synthesis results of the double beams: (a) numerically calculated, full-wave simulated, and experimentally measured beam patterns; (b) corresponding amplitude and phase of the array weighting vector. References to color refer to the online version of this figure

also composed of 30 elements. As shown by the black solid line in Fig. 5a, two main beams pointing to $-9°$ and $16°$ are formed. Moreover, the side lobe level is all less than -24 dB including the transition area. Fig. 5b shows the weighting factors of the array.

The optimization program is executed on a computer with Intel i5-8300H CPU (2.9 GHz) and 16 GB RAM. The time required for the three optimizations is 27.65, 31.96, and 15.34 s, and the memory consumption is 4.82, 46.2, and 7.45 MB, respectively.

3.2 Full-wave simulations and experimental measurements

The calculated weighting vectors are then physically implemented using reflective metasurface elements whose amplitudes and phases can be tailored independently. The structure of the metasurface element is shown in Fig. 6a, with a period of $W = 5$ mm. The structure consists of three layers, namely, the metallic ground, the 2-mm-thick substrate (F4B, ϵ_r=2.65, and tan δ=0.001), and the C-shaped metal (also called the split ring) on the top layer. The inner and outer radii of the ring are R_1=1.5 mm and R_2=2 mm, respectively. The opening angle of the ring is 2β, while the angle between the centerline of the ring and the x axis is α. As described in Bao et al. (2019), a y-polarized wave will be produced by the structure under the illumination of an x-polarized wave. It is noted that the propagation direction of incident electromagnetic waves is along the $-z$ axis. α and β are used to control the amplitude and phase of the reflected wave, respectively. By changing their values, we obtain waves with different amplitudes and phases, which can be used to embody the array weighting factors. Reflective metasurfaces

corresponding to cosecant, flat-top, and double beams are realized, separately. It is noted that linear arrays are copied as square arrays along the direction of the electric field in the full-wave simulations and experimental measurements. Fig. 6b shows one of the fabricated metasurfaces, which embodies the weighting vector shown in Fig. 3b and induces the cosecant beam.

The full-wave simulation results of the design giving rise to the cosecant beam are shown as the blue dashed line in Fig. 3a, from which we can see that the main lobe generally agrees with the numerical calculation. Although the side lobe level is slightly larger than the numerical calculation, it is still below −15 dB. The full-wave simulation results of the flat-top beam are represented as the blue dashed line in Fig. 4a. The main lobe here also agrees with the numerical calculation. Notably, there is a slightly high side lobe on the right side of the main lobe. The full-wave simulation results of the double-beam design are shown in Fig. 5a with the blue dashed line, whose main lobe coincides with the numerical calculation. The higher side lobes in Figs. 3a and 4a can be explained as follows: the numerical calculation is based on the point-source model, which is an ideal assumption. On the contrary, the full-wave simulations take actual physical mechanisms into account, such as the pattern of meta-atoms and the coupling between adjacent meta-atoms. Further work is demanded to include the physical mechanisms in the numerical calculation.

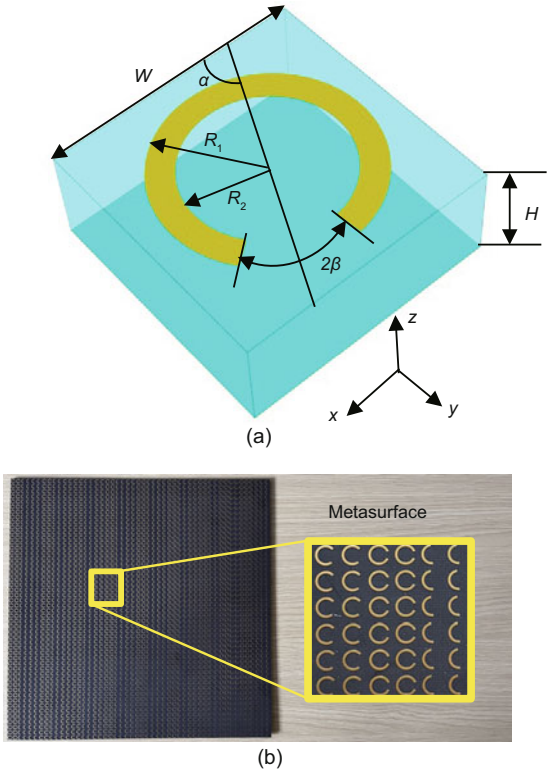

Fig. 6 The C-shaped metasurface element (a) and fabricated metasurface that gives rise to the cosecant beam (b)

Fig. 7 shows the scenario of measuring the beam patterns of the fabricated metasurfaces in a microwave anechoic chamber. The metasurfaces are fed by a horn antenna, and they are mounted at the center of a rotating stage. The recorded far-field patterns of the three designs are plotted as the red dotted lines in Figs. 3a, 4a, and 5a, separately. Overall, the beam patterns in the main lobe regions are in good agreement with those of full-wave simulations, although there is some growth of the side lobe level. The imperfection can be attributed to the influences of the drift of the dielectric parameter, the misalignment between the antenna and metasurface, and the errors in the fabrication. In general, the experimental results verify the feasibility of the numerical optimization method and the approach for realizing complex beams based on metasurfaces.

In this work, we use the cross-polarization conversion function of the C-shaped meta-atoms to verify the numerical algorithm. When we are controlling the magnitudes of the cross-polarized fields, part of the power becomes the co-polarized mode because the meta-atom is lossless. We analyze the co-polarized pattern of the three designs, and the results are given in Figs. S1–S3 in the supplementary materials. It is also preferable to give a quantitative comment on the gain of the designed metasurface, as shown in Figs. S4–S6 and Table S1 in

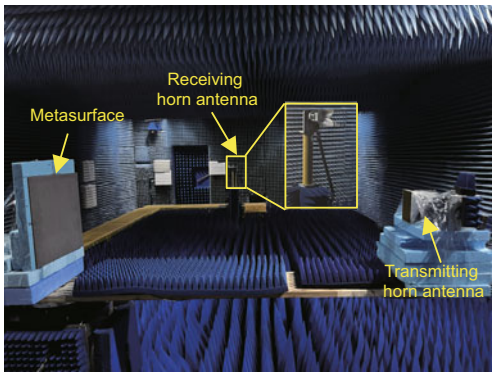

Fig. 7 Measurement scenario of the metasurface

the supplementary materials. The SDR algorithm is also applicable for synthesizing the pattern of two-dimensional (2D) arrays after vectorizing the beam steering matrix and visible optimization region. In light of this, the SDR algorithm sees no essential difference between the one-dimensional (1D) problem and 2D problem. The reason behind the fact that only 1D optimizations are shown in this work is that the rotator in our microwave anechoic chamber can rotate only horizontally, and we can measure only the beam pattern in one direction. Note that this study focuses on the application of the SDR method for the synthesis of complex beams, and the good agreement between the simulation and measurement patterns in the cross-polarization direction verifies the effectiveness of the method.

4 Conclusions

An effective approach for forming complex beams was presented. To find the optimal array weighting vector, the SDR technique was adopted to transform the non-convex optimization problem into a convex one, and the rank minimization theory was used iteratively. When there was no optimal solution, approximate results were obtained by using eigenvalue decomposition. Amplitude and phase coding metasurfaces composed of C-shaped rings were used to embody the optimized array weighting vector. The feasibility of the approach was verified by full-wave simulations and experimental measurements. Although this work considered only uniform linear arrays, it can be extended to the synthesis of planar and non-uniform arrays. The approach will find applications in the designs of wireless beamforming systems.

Contributors

Junwei WU designed the research. Junwei WU and Qiong HUA participated in the theoretical analysis and experimental designs, and drafted the paper. All the authors revised and finalized the paper.

Compliance with ethics guidelines

Tie Jun CUI is the editor-in-chief of this special issue, and Qiang CHENG is an executive lead editor of this special issue; they were not involved with the peer review process of this paper. All the authors declare that they have no conflict of interest.

Data availability

The data that support the findings of this study are available from the corresponding authors upon reasonable request.

References

Balanis CA, 2011. Modern Antenna Handbook. John Wiley & Sons, Hoboken, USA.

Bao L, Wu RY, Fu XJ, et al., 2019. Multi-beam forming and controls by metasurface with phase and amplitude modulations. *IEEE Trans Antenn Propag*, 67(10):6680-6685. https://doi.org/10.1109/TAP.2019.2925289

Boyd S, Vandenberghe L, 2004. Convex Optimization. Cambridge University Press, Cambridge, USA.

Bucci OM, D'Elia G, Mazzarella G, et al., 1994. Antenna pattern synthesis: a new general approach. *Proc IEEE*, 82(3):358-371. https://doi.org/10.1109/5.272140

Bucci OM, Caccavale L, Isernia T, 2002. Optimal far-field focusing of uniformly spaced arrays subject to arbitrary upper bounds in nontarget directions. *IEEE Trans Antenn Propag*, 50(11):1539-1554. https://doi.org/10.1109/TAP.2002.803959

Caorsi S, Massa A, Pastorino M, et al., 2005. Optimization of the difference patterns for monopulse antennas by a hybrid real/integer-coded differential evolution method. *IEEE Trans Antenn Propag*, 53(1):372-376. https://doi.org/10.1109/TAP.2004.838788

Cui TJ, Liu S, Zhang L, 2017. Information metamaterials and metasurfaces. *J Mater Chem C*, 5(15):3644-3668. https://doi.org/10.1039/C7TC00548B

Dolph CL, 1946. A current distribution for broadside arrays which optimizes the relationship between beam width and side-lobe level. *Proc IRE*, 34(6):335-348. https://doi.org/10.1109/JRPROC.1946.225956

Fazel M, Hindi H, Boyd S, 2004. Rank minimization and applications in system theory. Proc American Control Conf, p.3273-3278. https://doi.org/10.23919/ACC.2004.1384521

Grant M, Boyd S, 2020. CVX: Matlab Software for Disciplined Convex Programming, Version 2.2. http://cvxr.com/cvx [Accessed on Jan. 30, 2020].

Kajenski PJ, 2012. Phase only antenna pattern notching via a semidefinite programming relaxation. *IEEE Trans Antenn Propag*, 60(5):2562-2565. https://doi.org/10.1109/TAP.2012.2189709

Khodier MM, Christodoulou CG, 2005. Linear array geometry synthesis with minimum sidelobe level and null control using particle swarm optimization. *IEEE Trans Antenn propag*, 53(8):2674-2679. https://doi.org/10.1109/TAP.2005.851762

Lebret H, Boyd S, 1997. Antenna array pattern synthesis via convex optimization. *IEEE Trans Signal Process*, 45(3):526-532. https://doi.org/10.1109/78.558465

Li JY, Qi YX, Zhou SG, 2017. Shaped beam synthesis based on superposition principle and Taylor method. *IEEE Trans Antenn Propag*, 65(11):6157-6160. https://doi.org/10.1109/TAP.2017.2754468

Liang JC, Cheng Q, Gao Y, et al., 2022. An angle-insensitive 3-bit reconfigurable intelligent surface. *IEEE Trans Antenn Propag*, 70(10):8798-8808. https://doi.org/10.1109/TAP.2021.3130108

Lou Y, Jin L, Wang HM, et al., 2023. Multi-stream signals separation based on space-time-isomeric (spatio) array using metasurface antenna. *Sci China Inform Sci*, early access. https://doi.org/10.1007/s11432-023-3788-y

Luo ZQ, Ma WK, So AMC, et al., 2010. Semidefinite relaxation of quadratic optimization problems. *IEEE Signal Process Mag*, 27(3):20-34. https://doi.org/10.1109/MSP.2010.936019

Nai SE, Ser W, Yu ZL, et al., 2010. Beampattern synthesis for linear and planar arrays with antenna selection by convex optimization. *IEEE Trans Antenn Propag*, 58(12):3923-3930. https://doi.org/10.1109/TAP.2010.2078446

Palacios J, De Donno D, Widmer J, 2016. Lightweight and effective sector beam pattern synthesis with uniform linear antenna arrays. *IEEE Antenn Wirel Propag Lett*, 16:605-608. https://doi.org/10.1109/LAWP.2016.2594092

Shi L, Deng YK, Sun HF, et al., 2012. An improved real-coded genetic algorithm for the beam forming of space-borne SAR. *IEEE Trans Antenn Propag*, 60(6):3034-3040. https://doi.org/10.1109/TAP.2012.2194642

Strang G, 2023. Introduction to Linear Algebra. Wellesley-Cambridge Press, Wellesley MA, USA.

Sun S, Ma HF, Gou Y, et al., 2023. Spin- and space-multiplexing metasurface for independent phase controls of quadruplex polarization channels. *Adv Opt Mater*, 11(3):2202275. https://doi.org/10.1002/adom.202202275

Tsui KM, Chan SC, 2010. Pattern synthesis of narrowband conformal arrays using iterative second-order cone programming. *IEEE Trans Antenn Propag*, 58(6):1959-1970. https://doi.org/10.1109/TAP.2010.2046865

Wang F, Balakrishnan V, Zhou PY, et al., 2003. Optimal array pattern synthesis using semidefinite programming. *IEEE Trans Signal Process*, 51(5):1172-1183. https://doi.org/10.1109/TSP.2003.810308

Wu JW, Wang ZX, Fang ZQ, et al., 2020. Full-state synthesis of electromagnetic fields using high efficiency phase-only metasurfaces. *Adv Funct Mater*, 30(39):2004144. https://doi.org/10.1002/adfm.202004144

Wu JW, Wang ZX, Zhang L, et al., 2021. Anisotropic metasurface holography in 3-D space with high resolution and efficiency. *IEEE Trans Antenn Propag*, 69(1):302-316. https://doi.org/10.1109/TAP.2020.3008659

Wu JW, Wang ZX, Wu RY, et al., 2023. Simple and comprehensive strategy to synthesize Huygens metasurface antenna and verification. *IIEEE Trans Antenn Propag*, 71(8):6652-6666. https://doi.org/10.1109/TAP.2023.3283062

Yang F, Yang SW, Chen YK, et al., 2018. Convex optimization of pencil beams through large-scale 4-D antenna arrays. *IEEE Trans Antenn Propag*, 66(7):3453-3462. https://doi.org/10.1109/TAP.2018.2829875

List of supplementary materials

1 Co-polarization patterns

2 Gain of the metasurfaces

Table S1 Summary of the peak values of the scattered patterns

Fig. S1 Co-polarization pattern of the cosecant-beam metasurface

Fig. S2 Co-polarization pattern of the flat-top-beam metasurface

Fig. S3 Co-polarization pattern of the double-beam metasurface

Fig. S4 Scattered patterns of the cosecant-beam metasurface and an equal-size metal plate

Fig. S5 Scattered patterns of the flat-top-beam metasurface and an equal-size metal plate

Fig. S6 Scattered patterns of the double-beam metasurface and an equal-size metal plate